Research Article

Modelling the interaction between the p53 DNA-binding domain and the p28 peptide fragment of Azurin

Simona Santini[a], Anna Rita Bizzarri[a]* and Salvatore Cannistraro[a]

Recent experimental data reveal that the peptide fragment of Azurin called p28, constituted by the amino acid residues from 50 to 77 of the whole protein, retains both the Azurin cellular penetration ability and antiproliferative activity. p28 is hypothesized to act by stabilizing the well-known tumour suppressor p53 via a pathway independent from the oncogene Mdm2, which is the main p53 down-regulator, with its anticancer potentiality being probably connected with the binding of its amino acid residues 11 to 18 to p53. However, the p28 mode of action has not been completely elucidated yet, mostly because the details of the p28 interaction with p53 are still unknown. In the present study, computational docking modelling supported by cluster analysis, molecular dynamics simulations and binding free energy calculations have been performed to model the interaction between the DNA-binding domain (DBD) of p53 and the p28 fragment. Since the folding state of p28 when interacting with p53 inside the cell is not known, both the folded and the unfolded structures of this peptide have been taken into consideration. In both the cases, we have found that p28 is able to form with DBD a complex characterized by favourable negative binding free energy, high shape complementarity, and the presence of several hydrogen bonds at the interface. These results suggest that p28 might exert its anticancer action by hampering the binding of ubiquitin ligases to DBD, susceptible to promoting the p53 proteasomal degradation. Copyright © 2011 John Wiley & Sons, Ltd.

Keywords: p53; p28; docking; molecular dynamics; free energy

INTRODUCTION

The tumour suppressor p53, also called the guardian of the genome (Lane, 1992), is a potent transcription factor playing a crucial role in maintaining genome stability and preventing cancer development. As a key coordinator of cellular defence, p53 is a common denominator in human cancers, in most of which it is mutated (Harris, 1996; Vogelstein *et al.*, 2000; Veprintsev *et al.*, 2006; Greenblatt *et al.*, 1994) or its pathway altered (Clegg *et al.*, 2008). p53 is a homotetramer, and each monomer consists of 393 amino acid (aa) residues structured in three functional regions: an N-terminal domain (NTD, aa 1–93) involved in the p53 transcriptional function and growth suppression; a core DNA-binding domain (DBD, aa 102–292) responsible for site-specific DNA binding; and a C-terminal domain (CTD, aa 293–393) involved in the p53 tetramerization and in the regulation of the DBD function. The full-length p53 has not been crystallized, and only the structure of stable domains, such as the DBD and the tetramerization domain within the CTD, have been solved (Cho *et al.*, 1994; Clore *et al.*, 1994; Jeffrey *et al.*, 1995; Klein *et al.*, 2001).

In healthy cells, p53 is kept at low concentration by a feedback loop essentially mediated by the negative regulator protein Mdm2 (mouse double minutes 2), which is an E3 ubiquitin ligase that, upon binding to p53, blocks its transcriptional activity and promotes its proteasomal degradation (Levine, 1997; Haupt *et al.*, 1997; Brooks and Gu, 2006). In response to a broad range of stress signals, post-translational stabilization of p53 leads to an increase of its intracellular levels as well as to its activation, resulting in the gene transcription responsible for DNA repair, cell cycle arrest and apoptosis (Oren, 2003).

Due to its pivotal role in preventing the progression of tumours, p53 has become the focus of an avalanche of research aimed at identifying or designing molecules able to restore its activity, plausibly interfering with its down-regulation (Vassilev, 2004; Klein and Vassilev, 2004; Espinoza-Fonseca, 2005), and that can be then used in anticancer therapy.

In this respect, it has been found that Azurin, a copper-containing protein with electron transfer activity in *Pseudomonas aeruginosa*, plays a prominent anticancer role both *in vitro* (Yamada *et al.*, 2002a; Yamada *et al.*, 2002b; Goto *et al.*, 2003; Punj *et al.*, 2003; Punj *et al.*, 2004; Yamada *et al.*, 2004) and *in vivo* (Yamada *et al.*, 2002a; Punj *et al.*, 2004). Such an antiproliferative action has been shown to be consequent to the interaction of Azurin with p53 that leads to both the stabilization and the intracellular level rise of the transcription factor (Yamada *et al.*, 2002a; Yamada *et al.*, 2002b; Goto *et al.*, 2003; Punj *et al.*, 2003; Punj *et al.*, 2004; Yamada *et al.*, 2004). This interaction has been the object of many investigations in order to get insight into the relevant kinetic and molecular aspects. A single molecule atomic force spectroscopy experiment has shown that a stable complex is formed between full-length p53 and Azurin

* Correspondence to: Anna Rita Bizzarri, Biophysics and Nanoscience Centre, Facoltà di Scienze, Università della Tuscia, Largo dell'Università, 01100 Viterbo, Italy.
E-mail: bizzarri@unitus.it

S. Santini, A. R. Bizzarri, S. Cannistraro
Biophysics and Nanoscience Centre, CNISM, Facoltà di Scienze, Università della Tuscia, 01100 Viterbo, Italy

(Taranta *et al.*, 2008). Moreover, biological studies as well as computational methods have suggested that Azurin can bind either the NTD of p53 (Punj *et al.*, 2003; Punj *et al.* 2004; Apiyo and Wittung-Stafshede, 2005; Taranta *et al.*, 2009) or its DBD (Punj *et al.*, 2003; Punj *et al.*, 2004, Bizzarri *et al.*, 2009; De Grandis *et al.*, 2007). On the other hand, site-direct mutagenesis (Yamada *et al.*, 2002a; Goto *et al.*, 2003; Yamada *et al.*, 2004) as well as computational investigations (De Grandis *et al.*, 2007) have revealed that the two methionines located at positions 44 and 64 within a hydrophobic patch (HP) of Azurin and close to its copper atom in the active site are crucial for the interaction with p53.

Although Azurin is internalized efficiently and preferentially in cancerous with respect to normal cells (Yamada *et al.*, 2005), the protein could display some immunogenicity capable of inducing significant side effects, which may interfere with its pharmaceutical efficiency (Yamada *et al.*, 2002a).

In order to search for therapeutic molecules with the same cytotoxicity, delivery and target specificity as those of Azurin but with lesser side effects, peptides formed by suitably truncated portions of the Azurin have been investigated. Quite promising results have been obtained with a 2.9-kDa peptide fragment formed by the aa residues 50 to 77 of Azurin. This peptide, called p28 and encompassing the Azurin α-helix, has been shown to retain, *in vitro* and *in vivo*, not only the cellular penetration ability of the whole protein but also its antitumour activity (Yamada *et al.*, 2005; Taylor *et al.*, 2009; Yamada *et al.*, 2009; Mehta *et al.*, 2010). This antiproliferative action seems to be connected with the ability of the p28 aa residues from 11 to 18 to bind to p53. On the other hand, it has been observed that the peptide does not interfere with the Mdm2 ubiquitination pathway (Yamada *et al.*, 2009), so its mechanism of action appears to be different from that of Azurin.

However, the p28 mode of action has not been completely elucidated, essentially because the molecular details of its interaction with p53 have not been clarified yet. Therefore, a detailed study of the p28–p53 interaction could provide rewarding information on the p28 action at the molecular level and possibly might help refine the initial molecule in order to raise its anticancer potentialities. Hence, in the present study, we have used computational methods to disclose the possible formation of complexes between p28 and the DBD, paying particular attention to the molecular details of the peptide–protein interface. DBD is indeed a very important domain, not only for the p53 capability to bind DNA and then for its transcription activity, but also for the ubiquitination pathway, involving different proteins that are responsible for the proteasomal degradation of p53.

Since the folding state of p28 inside the cell is not known, we have taken into consideration two different starting structures for the peptide: (i) a folding structure derived from the crystallographic structure of Azurin and suitably relaxed by molecular dynamics (MD) simulation and (ii) an unfolded structure obtained by submitting the folded one to high-temperature cycles to mimic the structure obtained after synthesis.

Each of these two models of p28 (folded and unfolded) has been separately submitted to a docking procedure with the X-ray structure of the DBD. Docking has been then followed by cluster analysis, MD simulations and binding free energy calculations. We have found that both the folded and the unfolded p28 peptides can form complexes with the DBD, characterized by a rather low binding free energy, high interface complementarity

and several hydrogen bonds (HBs) at the interface. The occurrence of these complexes between p28 and p53–DBD is discussed in connection with the molecular mechanism of the anticancer action of the Azurin-derived peptide.

MATERIAL AND METHODS

p28

p28 is an amphipathic peptide formed by the aa residues from 50 to 77 of Azurin (LSTAADMEGVVTDGMASGLDKDYLKPDD), encompassing part of its HP; the peptide corresponds to a portion of the α-helix (aa residue 54 to 67) and to a part of a β-sheet of Azurin. Modelling of its structure is reported below.

DNA-binding domain

The DBD structure of p53 used in the docking procedure was derived from chain B of the Protein Data Bank (PDB) entry 1TUP (Figure 1), which provides a 2.2-Å resolution crystal structure of this domain complexed with a consensus DNA (Cho *et al.*, 1994). DBD is the only domain of p53 that was entirely crystallized; it consists of a β-sandwich formed by two antiparallel β-sheets, S_I and S_{II}, which are made up of four strands (S1, S3, S5 and S8) and five strands (S4, S6, S7, S9 and S10 N-terminal), respectively. The β-sandwich structure acts as a scaffold for the large L2 and L3 loops, and for a loop–sheet–helix motif (L1-S_{III}-H2) where sheet S_{III} is formed by S2–S2' β-hairpin and by the C-terminal of S10. The longer L2 loop (aa 163–195) is between the S4 and S5 β-strands, whereas the shorter L3 loop (aa 236–251) occurs between the S8 and S9 strands. Both loops have little secondary structure: L2 begins with a turn, which is followed by three segments interrupted only by the short helix H1; L3 contains three turns. The lack of extensive backbone HBs in these loops is compensated, in part, by the presence of a zinc atom, which is coordinated by the side chains of the residues Cys176, His179, Cys238 and Cys242 (Duan and Nilsson, 2006) and connects the two loops together. The functional binding to the DNA occurs within the L1 and L3 loops in a region that we have conventionally chosen to be the northern part of the molecule. In binding to DNA, the H2 helix and L1 loop fit into the DNA major groove while the L3 loop binds to the minor groove.
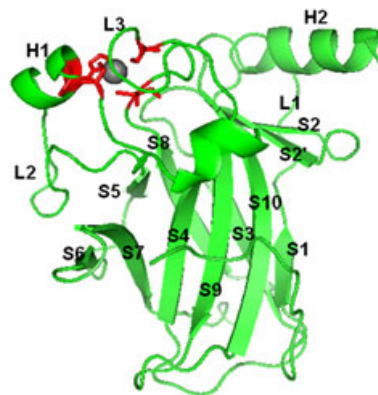

Figure 1. Three-dimensional structure of the p53 DBD (aa residues from 96 to 292), taken from chain B of PDB entry 1 TUP. The zinc in the northern part of the molecule is represented as a sphere while the residues coordinated to it are represented as sticks.

Protein docking

We employed Z-Dock (Chen and Weng, 2002; Chen and Weng, 2003), a rigid-body docking algorithm using Fast Fourier Transform to perform a six-dimensional search in the translational and rotational space between the two molecules, which would generate a set of possible models for both the DBD–p28F and DBD–p28UNF complexes, starting from the previously determined structures of the individual partners. Accordingly, each biomolecule is projected into a three-dimensional (3D) point grid of $128 \times 128 \times 128$ with a spacing of 1.2Å, representing the surface or the interior of the molecules. Z-Dock searches orientational space by rotating the ligand (p28) around its geometric centre, with the receptor (DBD) kept fixed in space. For each sampled rotational angle, which we fixed at 6°, only the ligand translations corresponding to the best geometric match between the two proteins were retained. In such a way, we obtained 2000 models for each complex, ranked on a scoring function combining shape complementarity, desolvation energy and electrostatics. To eliminate the similar structures generated by Z-Dock, we then used the ClusPro 1.0 (http://nrc.bu.edu/cluster/) docking server (Comeau *et al.*, 2004), which performs a cluster analysis by means of a pair-wise binding site using the root mean square displacements (RMSD) criterion. Models whose RMSD values, calculated for backbone atoms, differed by less than a clustering radius of 6Å were put in the same group. Then, only the first 15 models for each one of the two complexes were retained and analyzed by means of a 3D graphical inspection as well as by the protein–protein interaction server (Jones and Thornton, 1996). In such a way, we obtained detailed properties at the interface of each model, which helped us select the models to be subjected to further analysis, such as MD simulation and binding free energy calculation.

Molecular dynamics simulation

The binding models that emerged from the clustering procedure and from a suitable filtering process (see below) were subjected to MD simulation in water. The MD run was performed with the GROMACS 4.0.5-4 (http://www.gromacs.org/) (Hess *et al.*, 2008) package, using the GROMOS96 43a1 (http://www.gromacs.org/) forcefield (Van der Spoel *et al.*, 2001). Each model was solvated in a simple point charge water box (Berendsen *et al.*, 1969) extending to 1nm from the complex surface. All ionizable residues were assumed to be in the ionization states expected at pH 7 by taking into consideration their standard pKa values. A Na$^+$ counterion was added to the simulation box to keep the simulated systems neutral. The MD simulations were carried out in the isothermal-isobaric ensemble (NPT) ensemble with $T=300$K and $P=1$bar. The Nose–Hoover thermostat method was used to control the system temperature, with coupling time constant $\tau_T=0.1$psec (Nose's, 1984). Constant pressure was applied using the Parrinello–Rahman extended ensemble ($\tau_P=1.0$psec) (Parrinello and Rhaman, 1981). The long-range electrostatics was treated with the particle mesh Ewald method, with a lattice spacing of 1.2Å. A 9-Å cut-off was employed for Lennard–Jones interactions. The pair list was updated every 10 steps. All covalent bonds were constrained with the Linear Constraint Solver (LINCS) algorithm (Hess *et al.*, 1997). The time step was chosen to be 2fsec. The complexes were minimized with steepest descent and gradually heated from 50 to 300K, at 50-psec time intervals (150K in the first step and 50K in the second and third steps). The systems were then equilibrated by a 600-psec

MD simulation under harmonic position restraints of all heavy atoms with a force constant of 1000kJ/(molnm^2). Finally, an unrestrained MD run was carried out for 3nsec. The first 2nsec of the run was treated as a further equilibration simulation, and the remainder 1nsec was taken for data collection and for later binding free energy analysis.

Calculation of the binding free energy

The interaction free energies of the models that emerged from the MD simulations were evaluated with the molecular mechanics Poisson–Boltzmann surface area (MM-PBSA) method (Srinivasan *et al.*, 1998), which is an accurate and rapid procedure to estimate binding affinities of protein–protein complexes. The procedure is based on a combination of molecular mechanics and continuum solvent approach to evaluate the binding free energy of a protein complex, which in our case can be expressed as $G_{binding}=G_{DBD–p28} – G_{DBD} – G_{p28}$, where each term can be calculated as

$$G = E_{MM} - TS_{MM} + G_{solv} \qquad (1)$$

In Eqn (1), the free energy is split into a 'gas phase' term, containing the internal energy (E_{MM}), the entropic part (TS_{MM}) and the solvation contribution (G_{solv}); the three terms are averaged over a set of snapshots taken during the MD run for the complex, the DBD and the p28. The solvation term G_{solv} can be further decomposed into the electrostatic ($G_{polar,solv}$) and the non-polar ($G_{non-polar,solv}$) parts (Massova and Kollman, 1999). As it is commonly done in similar studies, we assumed that no changes occur in the receptor and ligand conformations upon binding (Taranta *et al.*, 2009; De Grandis *et al.*, 2007; Ganoth *et al.*, 2006).

The E_{MM} energy can be written as $E_{MM}=E_{elec}+E_{VdW}$, where the two terms represent the protein–protein electrostatic and Van der Waals interaction energies, respectively.

The entropic contribution to the free energy was evaluated using the approach developed in Andricioaei and Karplus (2001) and Basdevant *et al.* (2006). In particular, the configurational entropy was estimated using the quasi-harmonic analysis from the following expression:

$$S_{ho} = k_B \sum_{i=1}^{3N-6} \left[\frac{\gamma}{e\gamma/1} - ln\left(1 - e^{-\gamma}\right) \right]$$

where $\gamma = h/2\pi\sqrt{1/k_B T \lambda_i}$, h is the Planck constant, k_B is the Boltzmann constant, T is the absolute temperature and λ_i is the eigenvalues of the all-atom mass weighted covariance matrix of fluctuations $\sigma_{ij} = \sqrt{m_i m_j}\langle(x_i - \langle x_i\rangle)(x_j - \langle x_j\rangle)\rangle$. The structures used to compute the covariance matrix of fluctuations for each system were extracted from the same MD trajectories used for the MM-PBSA binding free energy calculations. Finally, the entropic contribution to the free energy was estimated by calculating the TS_{MM} term for the different docking models.

The electrostatic part of the solvation free energy was obtained by numerically solving the Poisson–Boltzmann equation with the Adaptive Poisson–Boltzmann Solver (APBS) (http://www.poissonboltzmann.org/apbs/) software (Wu *et al.*, 2004; Baker *et al.*, 2001). The grid spacing was set to 0.25Å. We used the GROMOS96 43a1 forcefield (Van der Spoel *et al.*, 2001) parameter set for atomic charges and radii, and a probe radius of 1.4Å to define the dielectric boundary. The inner dielectric constant for the complexes was 4, and the water

dielectric constant was set to 80 (Ganoth *et al.*, 2006). The non-polar contribution to G_{solv} was taken to be proportional to the solvent accessible surface area (SASA): $G_{non\text{-}polar,solv} = \gamma$ SASA $+ \beta$, with $\gamma = 2.2\,kJ/(mol\,nm^2)$ and $\beta = 3.84\,kJ/mol$ (Taranta *et al.*, 2009; De Grandis *et al.*, 2007; Chong *et al.*, 1999).

For each simulated model, all calculations (except for $G_{polar,solv}$ for which we used 10 snapshot structures) were averaged over 150 snapshot structures.

Figure preparation

The figures were created with Pymol (http://www.pymol.org/), a powerful molecular graphics system that has 3D capabilities (DeLano, 2002; Seeliger and De Groot, 2010).

RESULTS AND DISCUSSION

Modelling of p28

p28, synthesized as reported in Yamada *et al.* (2009), displays an unordered structure in water, as revealed by circular dichroism (CD) studies (personal communication from Prof. C. Beattie, University of Illinois, Chicago). However, it is known that small peptides passing across the cell membrane or put in a hydrophobic medium are in general able to fold (Lundberg and Langel, 2003; Lindberg and Gräslund, 2001; Magzoub *et al.*, 2003). Therefore, since the structure of p28 that was inside the cell and supposed to interact with the DBD is unknown, we separately subjected a folded (p28F) and an unfolded (p28UNF) form of p28 to a docking procedure with the DBD, which were derived as described in the following discussion.

To model the p28F structure, we started by cutting the corresponding portion of the X-ray structure of Azurin, chain B of PDB entry 4AZU (Nar *et al.*, 1991) (Figure 2A), and then relaxed it by carrying out an MD simulation in aqueous solution. This would release all the strains arising from bth the X-ray structure and the removal of the peptide from the Azurin structure as well as from placing it in water. In particular, this fragment was centred in a rectangular box with a dimension of $4.03\,nm \times 4.63\,nm \times 3.87\,nm$ and filled with 2372 water molecules, modelled by SPC (Berendsen *et al.*, 1969). To ensure the neutrality of the system, four Na^+ ions were added to the simulation box. After energy minimization and heating procedures, an MD simulation run was carried out for 30 nsec (for details, see discussion below). The temporal evolution of the RMSD for the C_α atoms from the initial structure, together with some snapshots during the run, is shown in Figure 2B. A significant increase in the RMSD, due to a partial unfolding of the α-helix structure, was observed within the first 3 nsec. Hereafter, the RMSD showed a marked decrease, which corresponds to a partial restoration of the α-helix; a concomitant formation of a ring between the C- and N-terminals giving rise to a β-sheet structure was also observed. A further slight increase of the α-helix portion was seen at about 23 nsec during the run. This structure was then maintained for longer times. The average over the last 100 psec of the MD run (Figure 2C) was the starting structure used in the docking procedure with DBD.

The p28UNF structure that was to be used in the docking procedure was obtained by starting from the structure resulting from the 30-nsec MD run previously described and subjecting it to a temperature increase from 300 to 400 K. A 6-nsec MD
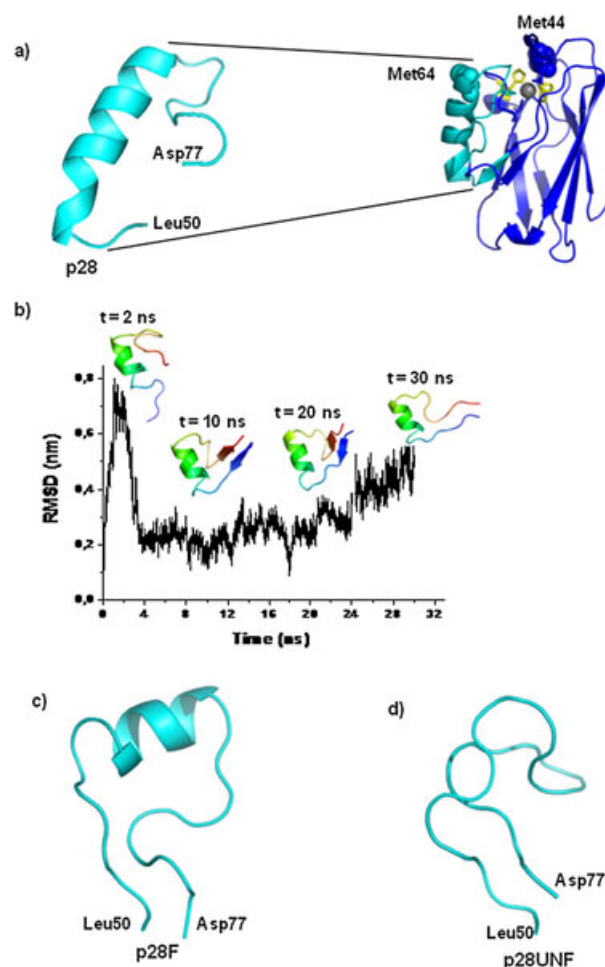

Figure 2. (A) Three-dimensional structure of Azurin (chain B of PDB entry 4 AZU) on the right. The copper atom in the northern part of the molecule and Met64 and Met44 are represented as spheres. Zoom-in image of the lighter region formed by the 50–77 amino acids involved in the α-helix and corresponding to p28 on the left. (B) Temporal evolution of the p28 C_α RMSD from the initial structure during the 30-nsec MD run, together with snapshots taken at 2 nsec, 10 nsec, 20 nsec and 30 nsec. (C) Three-dimensional structure of the p28 folded conformation (p28F). (D) Three-dimensional structure of the unfolded p28 conformation (p28UNF).

simulation was then performed; the resulting p28UNF structure is shown in Figure 2D.

Docking and molecular dynamics simulation

As mentioned in the Material and Methods section, the application of the Z-Dock algorithm generated 2000 possible models for both the DBD–p28F and the DBD–p28UNF complexes. After clustering by means of the ClusPro 1.0 docking server, the binding models were reduced to only 15 for both complexes. They were then filtered in order to accept those models in which (i) the DNA-binding region of DBD was not engaged in the interaction with the peptide (Yamada *et al.*, 2002a, Yamada *et al.*, 2009) and (ii) the aa residues from 11 to 18 of p28 were involved in binding to the DBD (Yamada *et al.*, 2009). Accordingly, the number of the possible models was further reduced to 11 for the DBD–p28F complex and to 13 for DBD–p28UNF.

A visual inspection of the 3D structure of these models revealed that both p28F and p28UNF bind essentially to three

distinct DBD regions: (i) the L1 loop or the strands close to it; (ii) the L2 loop; and (iii) the DBD southern part (the region responsible for the binding to DNA corresponds to the northern part of the biomolecule). The models have been thus grouped according to these three binding areas. Group I includes the models in which p28 binds to the DBD within a region close to the L1 loop. Two corresponding examples are shown in Figure 3A. Group II includes the models in which p28 binds to DBD at its L2 loop or nearby strands (see two examples in Figure 3B). Finally, group III collects the models in which p28 binds to the DBD southern region (Figure 3C). Model 15 for the DBD–p28UNF complex does not fall in this classification; with p28 binding to the DBD S5, S7 and S8 strands and S7–S8 loop.

The physical properties of the protein–protein interface relevant to the complex stability are reported in Tables 1 and 2. The accessible surface area (ASA) values, which are the difference in the water accessible surface area between the complex and the single proteins and provide information on the protein–protein geometric fit, are reported in the third column. These values, for both the DBD–p28F and the DBD–p28UNF models, are consistent with those expected for transient complexes (400–1000 Å^2) (Nooren and Thornton, 2003). Accordingly, a transient character could be suggested for the DBD–p28 interaction. The number of p28 residues at the complex interface (fourth column) ranges from 10 to 22, always involving an equivalent or slightly higher number of DBD residues (fifth column). Model 9 for the DBD–p28F interaction and model 6 for the DBD–p28UNF show the highest number of residues engaged in the interaction. Both the DBD–p28F and the DBD–p28UNF models are characterized by predominantly polar interfaces. Nevertheless, the difference in the polar and non-polar contribution is higher in the models of the DBD–p28F complex than in those of DBD–p28UNF (see the sixth and seventh columns of Tables 1 and 2). The number of HBs and salts bonds (SBs) at the interface
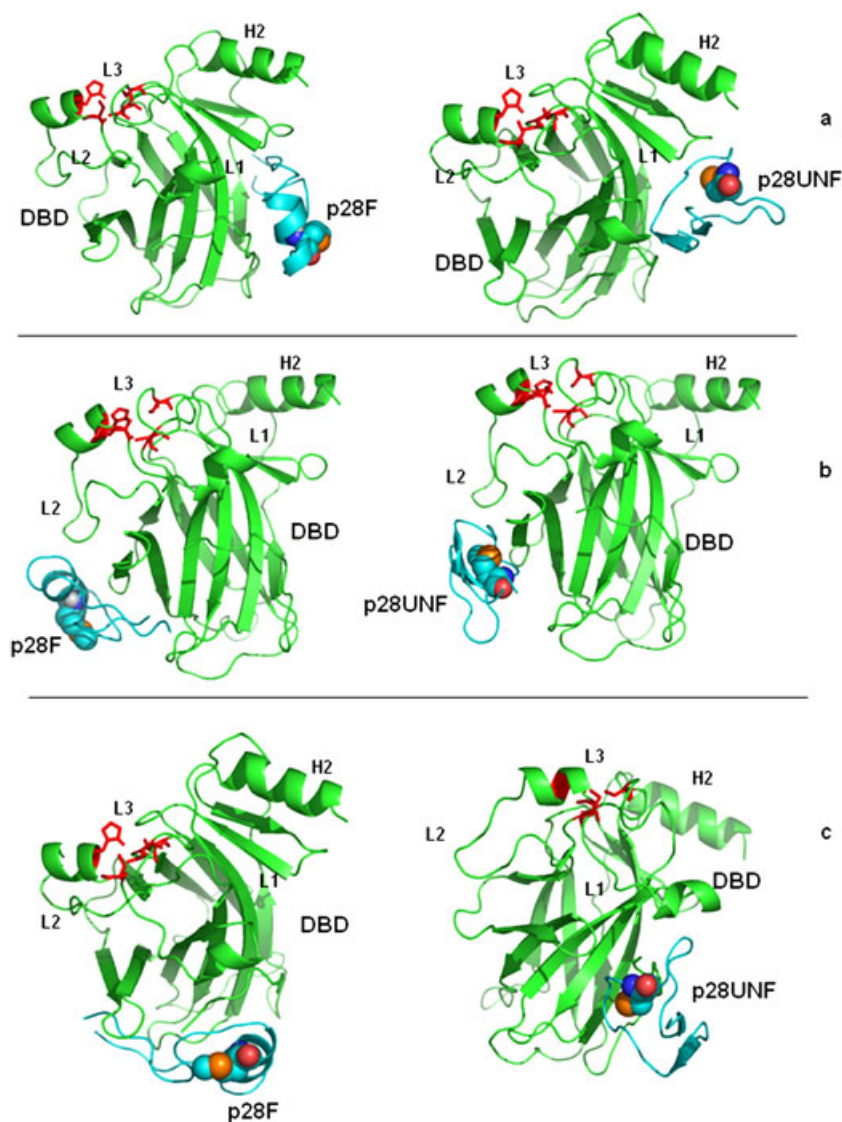
Figure 3. Three-dimensional structure of some docking models belonging to groups I, II and III. (A) Model 9 for the DBD–p28F complex (left) and model 9 for the DBD–p28UNF complex (right) of group I. (B) Model 7 for the DBD–p28F complex (left) and model 1 for the DBD–p28UNF complex (right) of group II. (C) Model 14 for the DBD–p28F interaction (left) and model 7 for the DBD–p28UNF interaction (right) for group III. In all the representations, Met15 of p28 (corresponding to Met64 of Azurin) is represented as spheres.

Table 1. Interface parameters of the 11 docking models for the DBD–p28F complex

Model	Group	ASA (Å^2)	p28 residues at interface	DBD residues at interface	% Polar residues at interface	% Non-polar residues at interface	HB/SB
Model 1	I	350	10	15	55	45	5/11
Model 2	I	608	15	25	70	40	5/10
Model 5	II	456	14	17	52	48	1/13
Model 6	I	507	13	19	58	42	3/16
Model 7	II	671	16	21	53	47	3/38
Model 9	I	818	22	26	62	38	6/10
Model 11	III	507	13	21	63	37	2/23
Model 12	I	479	14	18	64	36	2/12
Model 13	III	600	17	21	70	40	2/13
Model 14	III	696	19	24	62	38	6/20
Model 15	I	629	16	22	57	43	2/12

Parameters were evaluated by means of the PROTORP server.

(eighth column) is, on average, higher in the binding models for the DBD interaction with the unfolded p28 than in the models for the DBD–p28F complex. The models so far obtained are the result of a rigid docking modelling that does not take into account the effects of the protein flexibility and solvation.

To take into consideration the possible structural changes that the molecules may undergo upon binding, we carried out MD runs of the complexes extracted from the docking procedure. In particular, we performed a 3-nsec MD run of each complex in water (Taranta *et al.*, 2009; De Grandis *et al.*, 2007). During the MD simulation, the models underwent some conformational changes as witnessed by the temporal evolution of the corresponding RMSD for the C$_\alpha$ atoms from the crystallographic structure; two examples are shown in Figure 4A. In both cases, the RMSD increased during the first 1.5-nsec run, which was due to the relaxation of the complexes in water, and then it reached a plateau, indicative of the complex stabilization. The RMSD values for all the analyzed models, averaged over the last 1 nsec of the MD run, ranged from 1.8 to 2.6 Å for all the binding models (second column of Tables 3 and 4).

To determine the deviation of each residue from the initial structure, the RMSD of the C$_\alpha$ atoms for each model was calculated and plotted as a function of the residue number (Figures 4B and 4C). No large differences in the RMSD values were observed among the models, with the exception of model 5 for the DBD–p28F interaction and of model 4 for DBD–p28UNF, whose high RMSD values significantly deviate from all the others. Within each model, both the p28F and the p28UNF showed RMSD values significantly higher than those of the DBD; this was likely due to the smaller size of p28 with respect to DBD. Within DBD instead, the most significant fluctuations occurred at the level of residues belonging to unordered regions (i.e., residues 130–131 from the S7–S8 loop and residues 22–23 belonging to the L1 loop). In addition, among all the models, the highest RMSD values were shown by the DBD–p28UNF complexes, as evidenced by the single residue-averaged RMSD values reported in the third column of Tables 3 and 4.

Moreover, MD relaxation also yielded an increase in the complementarity of the two molecules as well as in the structure compactness as revealed by the SASA reduction that took place in almost all models, particularly in model 12 for the DBD–p28F complex and in model 3 for DBD–p28UNF (fourth and fifth columns of Tables 3 and 4).

Table 2. Interface parameters of the 13 docking models for the p53 DBD–p28UNF complex

Model	Group	ASA (Å^2)	p28 residues at interface	DBD residues at interface	% Polar residues at interface	% Non-polar residues at interface	HB/SB
Model 1	II	492	16	18	53	47	5/19
Model 2	III	655	14	23	63	37	6/26
Model 3	I	433	11	18	54	46	0/14
Model 4	I	463	15	15	60	40	1/23
Model 5	III	608	13	24	63	37	3/13
Model 6	III	745	18	25	61	39	11/30
Model 7	III	618	16	23	58	42	9/25
Model 9	I	665	18	24	54	46	3/35
Model 10	III	630	17	24	59	41	3/9
Model 11	I	644	16	19	54	46	3/18
Model 12	I	543	13	17	55	45	6/28
Model 14	I	566	15	15	54	46	3/28
Model 15	None	607	15	19	53	47	5/14

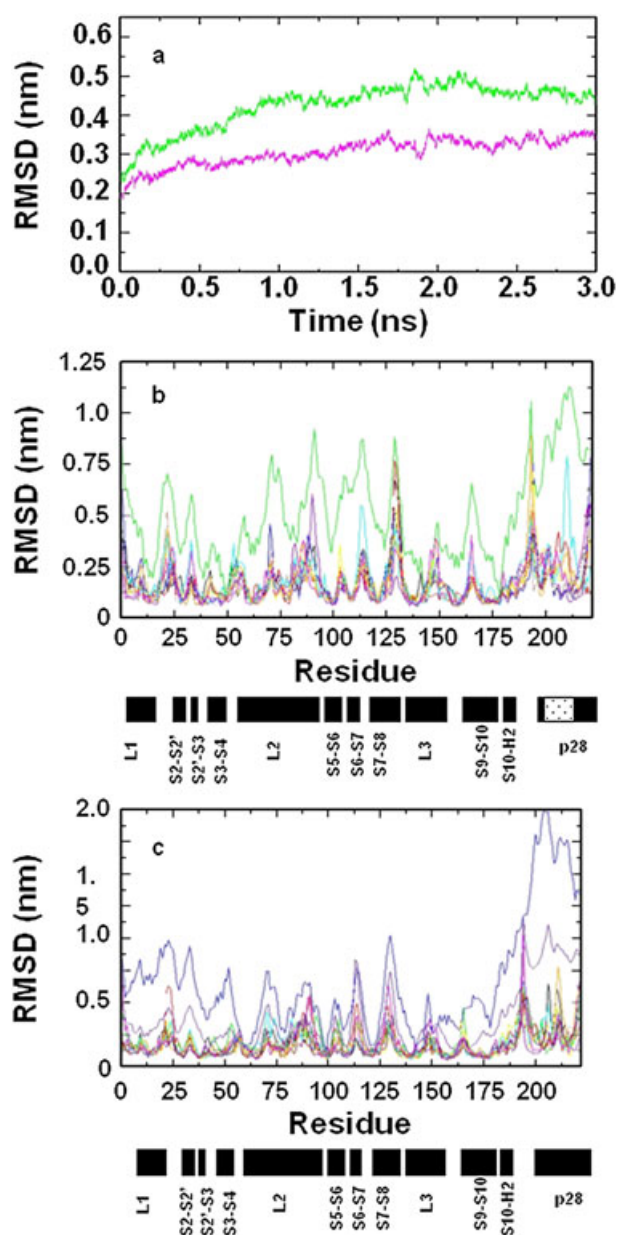Parameters were evaluated by means of the PROTORP server.

Figure 4. (A) Temporal evolution of the C_α RMSD from the crystallographic structure during the 3-nsec MD run for model 14 for the DBD–p28F complex (magenta line) and for model 3 for the DBD–p28UNF complex (green line). (B) RMSD from the crystallographic structure as a function of the residue number, averaged over the 1–3 nsec of the MD run for the 11 DBD–p28F models. Black line: model 1; red line: model 2; green line: model 5; blue line: model 6; yellow line: model 7; brown line: model 9; grey line: model 11; violet line: model 12; cyan line: model 13; magenta line: model 14; orange line: model 15. The black bars correspond to the DBD loops. DBD aa residues are from 1 to 194 while residues from 195 to 222 correspond to p28. The dotted bar under the graph underlines the p28 sequence corresponding to its α-helix. (C) RMSD as a function of the residue number, averaged over the 1–3 nsec of the MD run for the 13 DBD–p28UNF models. Black line: model 1; red line: model 2; green line: model 3; blue line: model 4; yellow line: model 5; brown line: model 6; grey line: model 7; violet line: model 9; cyan line: model 10; magenta line: model 11; orange line: model 12; navy line: model 14; black dotted line: model 15. The black bars correspond to the DBD loops and to the p28 aa residues. DBD residues come from 1 to 194 while the p28 residues come from 195 to 222.

Binding free energy calculation

To further search for the best complexes, the binding free energy of each model, as extracted from the docking procedure and refined by means of the MD simulation, was calculated by applying the MM-PBSA method. Such a procedure also allowed us to get some insight into the character of the binding forces driving the formation of each complex.

Generally, the $G_{binding}$ values are determined by the polar (G_{polar}) and non-polar ($G_{non-polar}$) free energies, which can in turn be decomposed in terms of the electrostatic and solvation contributions ($G_{polar}=E_{elec}+G_{polar,solv}$ and $G_{non-polar}=E_{VdW}+G_{non-polar,solv}$) and by the entropic term $T\Delta S$ (see Figures 5 and 6).

The calculation of the entropic contribution (bottom panels in Figures 5 and 6) gives rather low positive values (about 60 kJ/mol), which are very similar for both the DBD–p28F and DBD–p29UNF models, in agreement with what was observed for other protein–peptide interactions (Basdevant et al. 2006). At variance, both the polar and non-polar free energies (second and third panels in Figures 5 and 6) are characterized by high values and a marked variability among the various complexes.

From the final $G_{binding}$ values calculated for the 11 DBD–p28F models, shown in the upper panel of Figure 5, it turns out that models 2, 6, 9, 12, 13 and 14 display negative binding free energy values, while for the DBD–p28UNF complex (upper panel of Figure 6), negative $G_{binding}$ values were registered only for models 5, 6, 9 and 15. It should be noted that the lowest $G_{binding}$ values are displayed by model 13 ($G_{binding}=-635.9$ kJ/mol) for the DBD–p28F complex and by model 9 ($G_{binding}=-524.4$ kJ/mol) for DBD–p28UNF (see the last column of Table 5). We will therefore restrict our analysis only to these two models.

The $G_{binding}$ value of model 13 is mostly determined by the G_{polar} component (black bars in the middle panel of Figure 5) and, to a lesser extent, by the $G_{non-polar}$ component (black bars in the lowest panel of Figure 5). The foremost contribution to the polar free energy comes from its E_{elec} term, favourable to complex formation (white bars in the middle panel of Figure 5), while the solvation term, which tends to favour the unbound state, has an almost negligible value. The high contribution to the binding provided by the E_{elec} term finds a correspondence with the presence at the DBD–p28 interface of several polar residues (sixth column of Table 5). Also, the non-polar free energy is the result of the opposite contribution of its two terms, E_{VdW} and $G_{non-polar,solv}$. The favourable contribution of the E_{VdW} term (white bars in the lowest panel of Figure 5) dominates the unfavourable value of $G_{non-polar,solv}$ (grey bars in the lowest panel of Figure 5); this result is connected with the presence of hydrophobic residues at the interface (seventh column of Table 5).

For model 9, corresponding to the association of p28UNF with the DBD, the resulting $G_{binding}$ value arises mainly from the non-polar contribution to the binding and, to a lesser extent, from the polar contribution, as shown in the middle and lowest panels of Figure 6, respectively. The two terms of the polar free energy favour the binding process even if the contribution of the E_{elec} term is much higher than that of $G_{polar,solv}$, probably due to the polar character of the residues at the interface (sixth column of Table 5). The non-polar free energy instead comes from the E_{VdW} term (white bars in the lowest panel of Figure 6), which dominates over the unfavourable contribution to the binding arising from the $G_{non-polar,solv}$ term.

Therefore, both models 13 and 9 are essentially driven by the E_{elec} term of the G_{polar} component. This is different from what

Table 3. RMSD and SASA values for the 11 DBD–p28F models averaged over the MD simulation runs

Model	Time-averaged RMSD (Å)	Single residue–averaged RMSD (Å)	SASA (Å^2) before the MD run	SASA (Å^2) after the MD run
Model1	1.9 (0.2)	1.7 (1.0)	16192 (196)	15860 (263)
Model 2	1.9 (0.2)	1.5 (0.9)	15809 (348)	15514 (289)
Model 5	2.0 (0.1)	5.0 (2.2)	16051 (315)	15926 (410)
Model 6	2.3 (0.4)	1.7 (1.1)	15901 (213)	16077 (314)
Model 7	2.1 (0.1)	1.6 (0.9)	16045 (213)	15583 (261)
Model 9	2.0 (0.3)	1.5 (0.8)	15498 (255)	15413 (270)
Model 11	2.3 (0.4)	1.8 (1.1)	15983 (194)	15941 (274)
Model 12	2.0 (0.2)	1.5 (0.9)	16365 (226)	15524 (270)
Model 13	1.9 (0.2)	1.9 (1.1)	15783 (151)	15266 (282)
Model 14	2.1 (0.4)	1.7 (1.0)	15624 (166)	15776 (276)
Model 15	2.1 (0.3)	1.6 (0.9)	16370 (240)	15804 (304)

Standard deviation is reported in parentheses. SASA values after the MD run have been evaluated by averaging over the 2-to-3-nsec time interval of the MD run.

was observed for the DBD–Azurin interaction (De Grandis *et al.*, 2007), wherein the foremost contribution to the binding came from the $G_{non-polar}$ component and, specifically, from its E_{VdW} term, which was consistent with the high hydrophobic character of the DBD–Azurin interface. In connection with this, the DBD residues involved in the interaction with Azurin are listed in the last column of Table 7, from which we note that in the DBD–Azurin interaction, many more hydrophobic DBD aa residues are involved at the interface with respect to the DBD–p28 interaction.

Analysis of the best complexes between DNA-binding domain and p28

The 3D structures of model 13 for the DBD–p28F complex and of model 9 for DBD–p28UNF are shown on the left side of Figures 7A and 7B respectively. On the right side of the said figures, the corresponding details of the DBD–p28 interface are also shown, while all the p28 and the DBD aa residues involved in the two model complexes are listed in Tables 6 and 7. The

physical properties of the protein–protein interface of the two models, as obtained at the end of the MD simulation, are listed in Table 5 together with their $G_{binding}$ values.

Interestingly, both models display rather similar structures despite the fact that the modelling of the interaction of DBD was performed starting from two different structures for p28. According to model 13, the folded p28 binds at DBD sites that involve the N-terminal residues and the L2 loop of the latter , also with some contact with the S2–S2' loop (third and fourth columns of Table 7).

Model 9 shows that p28 binds to a DBD region located slightly to the north with respect to that of model 13, just within the level of the DBD S2–S2' loop (left side of Figure 7B). Nevertheless, the N-terminal DBD residues as well as the N-terminal residues of the L2 loop are at least in part involved in the interaction (fourth column of Table 7). In both models, the ASA values range from 540 to 620 Å^2 (third column of Table 5). These values, which were slightly lower than those observed before performing the MD run, are consistent with those expected for transient complexes (400–1000 Å^2). Again, in both models, more than half of the

Table 4. RMSD and SASA values for the 13 DBD–p28UNF models averaged over the MD simulation runs

Model	Time –averaged RMSD (Å)	Single residue-averaged RMSD (Å)	SASA (Å^2) before the MD run	SASA (Å^2) after the MD run
Model 1	2.0 (0.2)	1.9 (1.1)	15967 (242)	15745 (336)
Model 2	2.1 (0.3)	1.8 (1.1)	15985 (283)	15586 (295)
Model 3	2.1 (0.3)	1.9 (0.9)	16555 (159)	15651 (272)
Model 4	2.3 (0.2)	6.7 (2.4)	16391 (347)	15825 (348)
Model 5	2.0 (0.3)	1.5 (0.9)	15982 (182)	15830 (283)
Model 6	1.9 (0.4)	1.5 (0.7)	16060 (225)	15326 (260)
Model 7	2.6 (0.4)	2.0 (1.1)	15981 (275)	16189 (310)
Model 9	1.8 (0.2)	1.4 (0.6)	16104 (238)	15314 (274)
Model 10	2.0 (0.2)	1.8 (1.0)	16032 (177)	15828 (259)
Model 11	2.3 (0.4)	1.9 (1.3)	16235 (164)	15494 (287)
Model 12	2.0 (0.4)	1.7 (1.1)	15977 (217)	16251 (290)
Model 14	2.5 (0.6)	3.7 (2.4)	16516 (256)	15801 (282)
Model 15	1.8 (0.2)	1.6 (0.8)	16402 (183)	15865 (261)

Standard deviation is reported in parentheses. SASA values after the MD run have been evaluated by averaging over the 2-to-3-nsec time interval of the MD run.
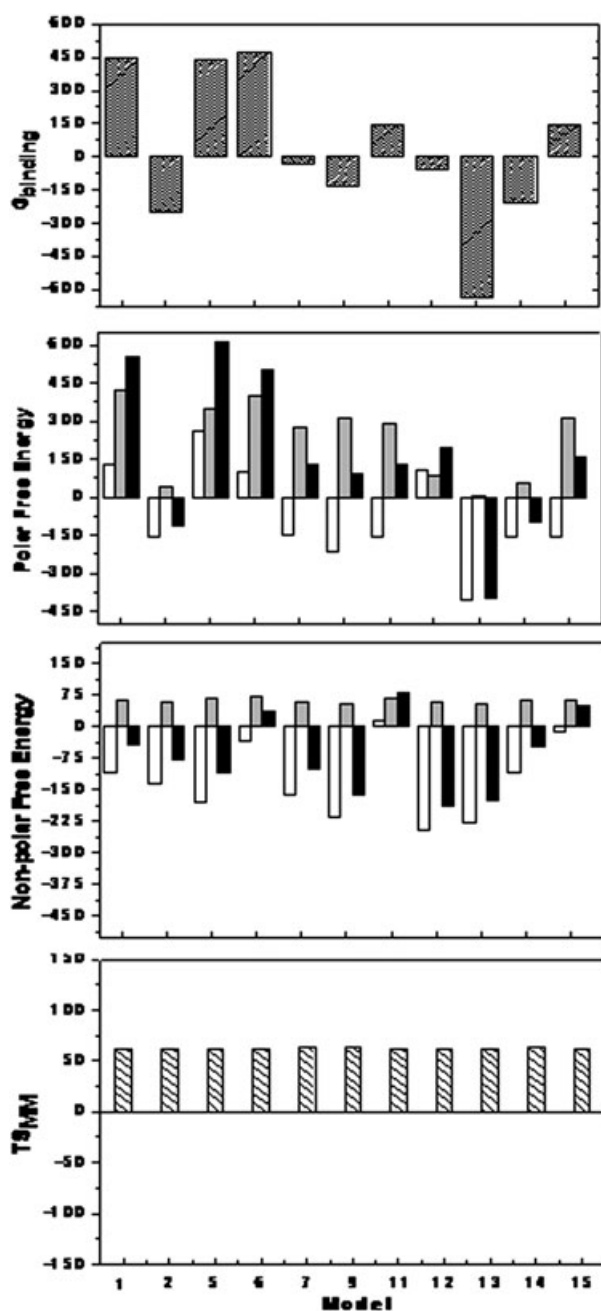
Figure 5. (Panels from top to bottom) The total binding free energy, the polar free energy (E_{elec}, $G_{polar,solv}$, $G_{polar}=E_{elec}+G_{polar,solv}$) and the non-polar contribution to the binding (E_{VdW}, $G_{non-polar,solv}$, $G_{non-polar}=E_{VdW}+G_{non-polar,solv}$) for the 11 DBD–p28F models. (Upper panel) $G_{binding}$ is in striped bars. (Middle panel) E_{elec} is in white, $G_{polar,solv}$ is in grey and G_{polar} is in black. (Lowest panel) E_{VdW} is in white, $G_{non-polar,solv}$ is in grey and $G_{non-polar}$ is in black. All the terms are expressed in kJ/mol.

Figure 6. (Panels from top to bottom) The total binding free energy, the polar free energy (E_{elec}, $G_{polar,solv}$, $G_{polar}=E_{elec}+G_{polar,solv}$) and the non-polar contribution to the binding (E_{VdW}, $G_{non-polar,solv}$, $G_{non-polar}=E_{VdW}+G_{non-polar,solv}$) for the 13 DBD–p28UNF models that emerged from the MD simulation. (Upper panel) $G_{binding}$ is shown in striped bars. (Middle panel) E_{elec} is in white, $G_{polar,solv}$ is in grey and G_{polar} is in black. (Lowest panel) E_{VdW} is in white, $G_{non-polar,solv}$ is in grey and $G_{non-polar}$ is in black. All the terms are expressed in kJ/mol.

p28 aa residues are involved in the interaction and are in contact with almost an equal number of DBD residues (fourth and fifth columns of Table 5). All models show a mostly polar interface (sixth and seventh columns of Table 5). In both models, the DBD–p28 interaction is stabilized by quite a high number of HBs and SBs (eighth column of Table 5). In particular, the four HBs at the DBD–p28F interface in model 13 (Figure 7A) are established among the p28 aa residues that are located at the N- and
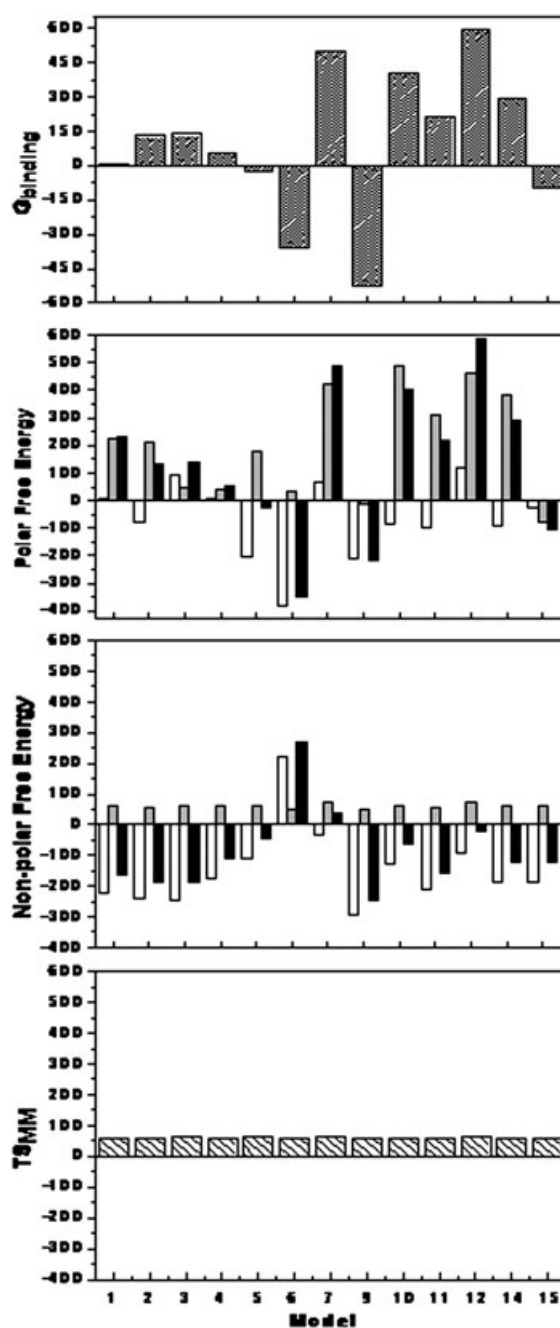
C- terminals of the peptide on one hand and the DBD aa residues belonging to its N-terminal and L2 loop on the other (see the legend to Figure 7 for details). In model 9, we can count nine p28UNF residues forming HBs with DBD; this is almost the same number of residues found stabilizing the DBD–p28F interaction in model 13, but the DBD residues engaged in these HBs are different (see the legend to Figure 7 for details). Such a high

1051

Table 5. Interface parameters and $G_{binding}$ values of model 13 for the DBD–p28F interaction and of model 9 for the DBD–p28UNF complex

	Model	Group	ASA (Å²)	p28 residues at interface	DBD residues at interface	% Polar residues at interface	% Non-polar residues at interface	HB/SB	$G_{binding}$ (kJ /mol)
DBD–p28F	Model 13	III	544	18	15	59	41	4/3	−635.9
DBD–p28UNF	Model 9	I	614	15	22	58	42	9/13	−524.4

The interface parameters were evaluated by means of the PROTORP server.

number of total HBs between the DBD and the small peptide p28, involving about one-third of the p28UNF residues engaged in the interaction, certainly indicates a very specific binding interaction.

By analyzing the p28 residues located at the protein–protein interface, we can observe that, in model 13, almost all the p28 aa residues from 11 to 18, which have been indicated by experiments to be responsible for the p28 binding to p53 (Yamada *et al.*, 2009), are involved in the interaction (second and third columns of Table 6). On the other hand, for the interaction of DBD with the unfolded p28, model 9 shows the highest ASA value and the highest number of HBs, SBs and aa residues involved at the interface.

In summary, our computational docking study suggests that both the folded and unfolded p28 peptide can form a complex with DBD with low binding free energy and high interface complementarity.

CONCLUSIONS

Computational docking supported by cluster analysis, MD simulations and binding free energy calculations has been applied to investigate the interaction between the DBD of p53 and the p28 peptide fragment of Azurin; for the latter, both a folded and an unfolded structure has been taken into consideration. Remarkably, in both these cases, we found that p28 and DBD undergo a molecular association characterized by low binding free energy, high shape complementarity, high number of stabilizing HBs, predominant polar interfaces and several engaged p28 aa
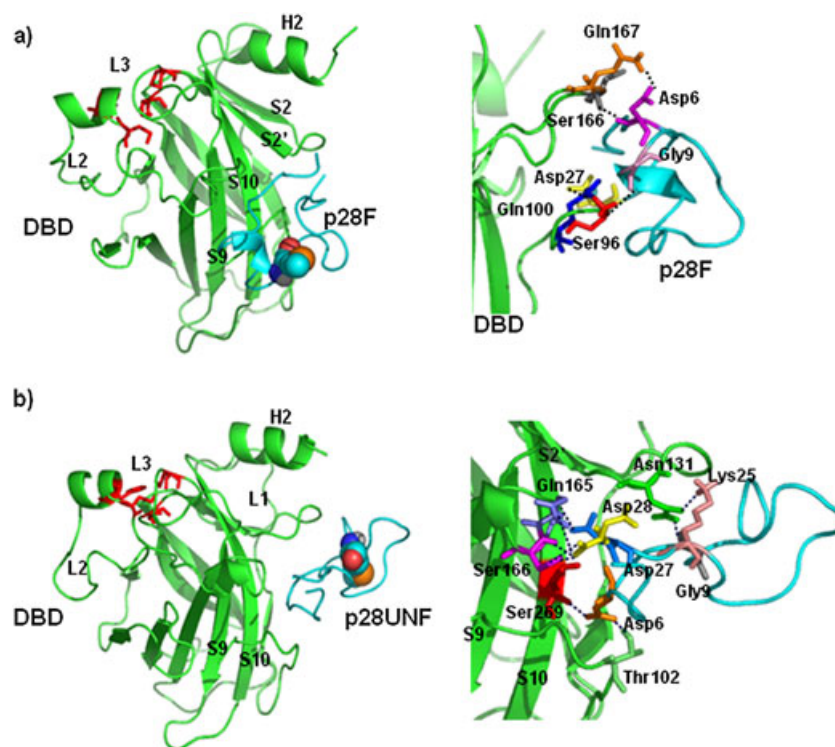

Figure 7. (A) Three-dimensional structure of model 13 for the DBD–p28F interaction after the MD run on the left, with a zoom-in image of the HB network at the binding interface on the right. In detail, the HBs at the interface are DBD Ser96–p28 Gly9, DBD Gln100–p28 Asp27, DBD Ser166–p28 Asp6 and DBD Gly167–p28 Asp6. (B) Model 9 for the DBD–p28UNF interaction after the MD run on the left and the HB network at the binding interface on the right. The HBs at the interface are DBD Thr102–p28 Asp6, DBD Asn131–p28 Lys25 and Gly9, DBD Gln165–p28 Asp28 and Asp27, DBD Ser 166 forms three bonds with the p28 Asp28 and DBD Ser269–p28 Asp6. In each figure, DBD and p28 are depicted in cartoon representations, while the intermolecular HBs are drawn as black dashed lines.

Table 6. p28 residues involved in the interaction with the DBD for the two best models that emerged from the binding free energies calculation are shaded in grey

p28 residues		DBD–p28F Model 13	DBD–p28UNF Model 9
Leu	1	■	■
Ser	2		
Thr	3	■	
Ala	4	■	■
Ala	5	■	■
Asp	6	■	■
Met	7		■
Gln	8	■	■
Gly	9	■	■
Val	10	■	■
Val	11	■	■
Thr	12		
Asp	13	■	■
Gly	14	■	■
Met	15	■	
Ala	16	■	
Ser	17	■	
Gly	18		
Leu	19		
Asp	20		
Lys	21		
Asp	22		
Tyr	23	■	■
Leu	24	■	
Lys	25	■	■
Pro	26		
Asp	27	■	■
Asp	28	■	■

Table 7. DBD residues involved in the interaction with p28 for the two best models emerged from the calculation of the binding free energy are shaded in grey

Elements of DBD structure	DBD residues		DBD–p28F Model 13	DBD–p28UNF Model 9	Azurin
N-terminal DBD residues	Ser	96	■		
	Val	97	■		
	Pro	98			
	Ser	99			
	Gln	100	■	■	
	Lys	101	■		
	Thr	102			
	Tyr	103	■		
	Gln	104		■	
S1 strand	Arg	110		■	■
	Leu	111		■	■
	Gly	112			■
L1 loop	Phe	113			■
	Leu	114			■
	His	115		■	■
	Ser	116			■
	Gly	117			■
	Thr	118			■
	Ala	119			■
	Val	122			■
S2 strand	Thr	125			■
S2–S2′ loop	Tyr	126		■	■
	Pro	128	■		
	Ala	129	■	■	■
	Leu	130	■	■	
	Asn	131			■
S3 strand	Cys	141			
	Gln	144			■
	Trp	146			■
L2 loop	Lys	164	■	■	
N-terminal residues	Gln	165		■	
	Ser	166	■	■	
	Gln	167			
	Met	169	■	■	
	Thr	170	■		
S6–S7 loop	Asp	208			
	Asn	210			
S7–S8 loop	Asp	228			■
	Cys	229			■
S9 strand	Arg	249		■	
N-terminal residues	Leu	252		■	
S9–S10 loop	Ser	261			
	Gly	262			
	Asn	263			
S10 strand	Leu	264			
	Arg	267		■	
	Asn	268		■	
	Ser	269		■	
	Phe	270		■	
	Glu	271			
H2 helix	Arg	282			■
	Arg	283			■
	Glu	286			■
C-terminal DBD residues	Gly	287			■
	Leu	289			■

In the last column, the DBD residues bound by Azurin as predicted in De Grandis et al., (2007) are also shown as shaded boxes.

residues (up to 80%). Strikingly enough, the structures of the two complexes are rather similar, with p28 preferentially binding at DBD sites involving both the N-terminal residues and L2 loop of the latter, together with some contact with the S2–S2′ loop. These results suggest that both the folded and unfolded structures of p28 can form a stable complex with DBD. It could then be very important to disclose the effective structure of p28 when it interacts with p53 within the cellular environment; in this respect, nuclear magnetic resonance experiments could be of great help. Moreover, since the p28 aa residues from 11 to 18 seem to be essential to the p28–p53 interaction, it could be interesting to test the effects that their mutations might have on the stability of the DBD–p28 complex. In this respect, Val11, Asp13 and Gly14, which are all involved in both best models, could be the preferential target of such a mutagenesis investigation.

The occurrence of complexes between the DBD and p28 peptide fragment of Azurin allows us to hypothesize that the p28 anticancer potentiality might be connected with its ability to hamper the binding of ubiquitin ligases (such as COP1, Pirh2 and perhaps TOPORS and ARF-BP1) (Chan *et al.*, 2006; Rajendra *et al.*, 2004; Chen *et al.*, 2005; Dornan *et al.*, 2004; Corcoran *et al.*, 2004) to DBD by preventing in such a way the tumour suppressor p53 from a proteasomal degradation. Interestingly, it should be noted that p28, even though it retains the antiproliferative action of the whole

Azurin to which it belongs, displays a different molecular interaction with DBD (De Grandis *et al.*, 2007) and that this probably finds some correspondence with the claimed different biological anticancer pathway displayed (Yamada *et al.* 2009).

REFERENCES

Andricioaei I, Karplus M. 2001. On the calculation of entropy from covariance matrices of the atomic fluctuations. *J. Chem. Phys.* **115**: 6289–6292.

Apiyo D, Wittung-Stafshede P. 2005. Unique complex between bacterial Azurin and tumor-suppressor protein p53. *Biochem. Biophys. Res. Commun.* **332**: 965–968.

Baker NA, Sept D, Joseph S, Holst MJ, McCammon JA. 2001. Electrostatics of nanosystems: application to microtubules and the ribosome. *Proc. Natl. Acad. Sci. USA* **98**: 010037–10041.

Basdevant N, Weinstein H, Ceruso M. 2006. Thermodynamic Basis for Promiscuity and Selectivity in Protein-Protein Interactions: PDZ Domains, a Case Study. *J. Am. Chem. Soc.* **128**: 12766–12777.

Berendsen HJC, Postma JPM, Van Gunsteren WF, Hermans J. 1969. Interaction models for water in relation to protein hydration. *Nature* **224**: 175–177.

Bizzarri AR, Di Agostino S, Andolfi L, Cannistraro S. 2009. A Combined Atomic Force Microscopy Imaging and Docking Study to Investigate the Complex Between p53 DNA Binding Domain and Azurin. *J. Mol. Recognit.* **22**: 506–15.

Brooks CL, Gu W. 2006. p53 ubiquitination: Mdm2 and beyond. *Mol. Cell* **21**: 307–315.

Chan WM, Mak MC, Fung TK, Lau A, Siu WY, Poon RYC. 2006. Ubiquitination of p53 at multiple sites in the DNA-binding domain. *Mol. Cancer Res.* **4**: 15–25.

Chen R, Weng Z. 2002. Docking unbound proteins using shape complementarity, desolvation, and electrostatics. *Proteins: Struct. Funct. Genet.* **47**: 281–294.

Chen R, Weng Z. 2003. A novel shape complementarity scoring function for protein-protein docking. *Proteins: Struct. Funct. Genet.* **51**: 397–408.

Chen D, Kon N, Li M, Zhang W, Qin J, Gu W. 2005. ARF-BP1/Mule is a critical mediator of the ARF tumor suppressor. *Cell* **121**: 1071–1083.

Cho Y, Gorina S, Jeffrey PD, Pavletich NP. 1994. Crystal structure of a p53 tumor suppressor–DNA complex: understanding tumorigenic mutations. *Science* **265**: 346–355.

Clegg HV, Itahana K, Zhang Y. 2008. Unlocking the Mdm2-p53 loop: Ubiquitin is the key. *Cell Cycle* **7**: 287–292.

Clore GM, Omichinski JG, Sakaguchi K, Zambrano N, Sakamoto H, Appella E, Gronenborn AM. 1994. High-resolution structure of the oligomerization domain of p53 by multidimensional NMR. *Science* **265**: 386–391.

Comeau SR, Gatchell DW, Vajda S, Camacho CJ. 2004. ClusPro: a fully automated algorithm for protein–protein docking. *Nucleic Acids Res.* **32**: 96–99.

Corcoran C, Huang Y, Sheikh M. 2004. The p53 paddy wagon: COP1, Pirh2 and MDM2 are found resisting apoptosis and growth arrest. *Cancer Biol. Ther.* **3**: 721–725.

Chong LT, Duan Y, Wang L, Massova I, Kollman PA. 1999. Molecular dynamics and free-energy calculations applied to affinity maturation in antibody 48G7. *Proc. Natl. Acad. Sci. USA* **96**: 14330–14335.

DeLano WL. 2002. The PyMOL molecular graphics system. http://www.pymol.org

De Grandis V, Bizzarri AR, Cannistraro S. 2007. Docking study and free energy simulation of the complex between p53 DNA – binding domain and Azurin. *J. Mol. Recognit.* **20**: 215–226.

Dornan D, Bheddah S, Newton K, Ince W, Frantz GD, Dowd P, Koeppen H, Dixit VM, French DM. 2004. COP1, the negative regulator of p53, is overexpressed in breast and ovarian adenocarcinomas. *Cancer Res.* **64**: 7226–7230.

Duan J, Nilsson L. 2006. Effect of Zn^{2+} on DNA recognition and stability of the p53 DNA-binding domain. *Biochemistry* **45**: 7483–7492.

Espinoza-Fonseca LM. 2005. Targeting MDM2 by the small molecule RITA: Towards the development of new multi-target drugs against cancer. *Theor. Biol. Medical Modelling* **2**.

Ganoth A, Friedman R, Nachliel E, Gutman M. 2006. A molecular dynamics study and free energy analysis of complexes between the Mlc1p protein and two IQ motif peptides. *Biophys. J.* **91**: 2436–2450.

Goto M, Yamada T, Kimbara K, Horner J, Newcomb M, Das Gupta TK, Chakrabarty AM. 2003. Induction of apoptosis in macrophages by Pseudomonas Aeruginosa Azurin: tumour-suppressor protein p53 and reactive oxygen species, but not redox activity, as critical elements in cytotoxicity. *Mol. Microbiol.* **47**: 549–559.

Greenblatt MS, Bennett WP, Hollstein M, Harris CC. 1994. Mutations in the p53 tumor suppressor gene: clues to cancer etiology and molecular pathogenesis. *Cancer Res.* **54**: 4855–4878.

Harris CC. 1996. Structure and function of the p53 tumor suppressor gene: clues for rational cancer therapeutic strategies. *J. Natl. Cancer Inst.* **88**: 1442–1455.

Haupt Y, Maya R, Kazaz A, Oren M. 1997. Mdm2 promotes the rapid degradation of p53. *Nature* **387**: 296–299.

Hess B, Kutzner C, Van der Spoel D, Lindahl E. 2008. GROMACS 4: algorithms for highly efficient, load-balanced, and scalable molecular simulation. *J. Chem. Theor. Comput.* **4**: 435–447.

Hess B, Bekker H, Berendsen HJC, Fraaije JGEM. 1997. LINCS: a linear constraint solver for molecular simulations. *J. Comp. Chem.* **18**: 1463–1472.

Jeffrey PD, Gorina S, Pavletich NP. 1995. Crystal structure of the tetramerization domain of the p53 tumor suppressor at 1.7 angstroms. *Science* **267**: 1498–1502.

Jones S, Thornton JM. 1996. Principles of protein-protein interactions derived from structural studies. *Proc Natl Acad Sci USA* **93**: 13–20.

Klein C, Vassilev LT. 2004. Targeting the p53-MDM2 interaction to treat cancer. *Br. J. Cancer* **91**: 1415–9.

Klein C, Planker E, Diercks T, Kessler H, Kunkele KP, Lang K, Hansen S, Schwaiger M. 2001. NMR spectroscopy reveals the solution dimerization interface of p53 core domains bound to their consensus DNA. *J. Biol. Chem.* **276**: 49020–49027.

Lane DP. 1992. Cancer. p53, guardian of the genome. *Nature* **358**: 15–16.

Levine AJ. 1997. p53, the cellular gatekeeper for growth and division. *Cell* **88**: 323–331.

Lindberg M, Gräslund A. 2001. The position of the cell penetrating peptide penetration in SDS micelles determined by NMR. *FEBS Lett.* **497**: 39–44.

Lundberg P, Langel Ü. 2003. A brief introduction to cell-penetrating peptides. *J. Mol. Recogn.* **16**: 227–233.

Magzoub M, Eriksson LE, Gräslund A. 2003. Comparison of the interaction, positioning, structure induction and membrane perturbation of cell-penetrating peptides and non-translocating variants with phospholipid vesicles. *Biophys. Chem.* **103**: 271–288.

Massova I, Kollman PA. 1999. Computational alanine scanning to probe protein-protein interactions: a novel approach to evaluate binding free energies. *J. Am. Chem. Soc.* **121**: 8133–8143.

Mehta RR, Hawthorne M, Peng X, Shilkaitis A, Mehta RG, Beattie CW, Das Gupta TK. 2010. A 28-amino-acid peptide fragment of the cupredoxin Azurin prevents carcinogen-induced mouse mammary lesions. *Cancer Prev Res* **3**: 1351–1360.

Nar H, Messerschmidt A, Huber R, van de Kamp M, Canters GW. 1991. Crystal structure analysis of oxidized Pseudomonas aeruginosa Azurin at pH 5.5 and pH 9.0. A pH-induced conformational transition involves a peptide bond flip. *J. Mol. Biol.* **221**: 765–772.

Nooren IMA, Thornton JM. 2003. Structural characterization and functional significance of transient protein-protein interactions. *J. Mol. Biol.* **325**: 991–1018.

Nose' S. 1984. A molecular dynamics method for simulations in the canonical ensemble. *Mol. Phys.* **52**: 255–268.

Oren M. 2003. Decision making by p53: life, death and cancer. *Cell Death Diff.* **10**: 431–442.

Parrinello M, Rahman A. 1981. Polymorphic transitions in single crystals: a new molecular dynamics method. *J. Appl. Phys.* **52**: 7182–7190.

Punj V, Das Gupta TK, Chakrabarty AM. 2003. Bacterial cupredoxin Azurin and its interactions with the tumor suppressor protein p53. *Biochem. Biophys.* **312**: 109–114.

Punj V, Bhattacharyya S, Saint-Dic D, Vasu C, Cunningham EA, Graves J, Yamada T, Constantinou AI, Christov K, White B, Li G, Majumdar D, Chakrabarty AM, Das Gupta TK. 2004. Bacterial cupredoxin Azurin as an inducer of apoptosis and regression in human breast cancer. *Oncogene* **23**: 2367–2378.

Rajendra R, Malegaonkar D, Pungaliya P, Marshall H, Rasheed Z, Brownell J, Liu LF, Lutzker S, Saleem A, Rubin EH. 2004. Topors functions as an E3 ubiquitin ligase with specific E2 enzymes and ubiquitinates p53. *J. Biol. Chem.* **279**: 36440–36444.

Seeliger D, De Groot BL. 2010. Ligand docking and binding site analysis with PyMOL and Autodock/Vina. *J. Comput. Aided Mol. Des.* **24**: 417–422.

Srinivasan J, Cheatham TE, Cieplak P, Kollman PA, Case DA. 1998. Continuum solvent studies of the stability of DNA, RNA, and phosphoramidate—DNA helices. *J. Am. Chem. Soc.* **120**: 9401–9409.

Taylor BN, Mehta RR, Yamada T, Lekmine F, Christov K, Chakrabarty AM, Green A, Bratescu L, Shilkaitis A, Beattie CW, Das Gupta TK. 2009. Noncationic peptides obtained from Azurin preferentially enter cancer cells. *Cancer Res.* **69**: 537–546.

Taranta M, Bizzarri AR, Cannistraro S. 2008. Probing the interaction between p53 and the bacterial protein Azurin by single molecule force spectroscopy. *J. Mol. Recognit.* **21**: 63–70.

Taranta M, Bizzarri AR, Cannistraro S. 2009. Modelling the interaction between the N-terminal domain of the tumor suppressor p53 and Azurin. *J. Mol. Recognit.* **22**: 215–222.

Van der Spoel D, van Buuren AR, Apol E, Meulenhoff PJ, Tieleman DP, Sijbers A, Hess B, Feenstra KA, Lindahl E, van Drunen R, Berendsen HJC. 2001. GROMACS User Manual. University of Groningen: Groningen, The Netherlands, Version 3.2.

Vassilev LT. 2004. Small-molecule inhibitors of p53-MDM2 binding: research tools and potential cancer therapeutics. *Cell Cycle* **3**: 419–421.

Veprintsev DB, Freund SMV, Andreeva A, Rutledge SE, Tidow H, Pérez Cañadillas JM, Blair CM, Fersht AR. 2006. Core domain interactions in full-length p53 in solution. *Proc. Natl. Acad. Sci. USA* **103**: 2115–2119.

Vogelstein B, Lane D, Levine AJ. 2000. Surfing the p53 network. *Nature* **408**: 307–310.

Wu Y, Cao Z, Yi H, Jiang D, Mao X, Liu H, Li W. 2004. Simulation of the interaction between ScyTx and small conductance calcium-activated potassium channel by docking and MM-PBSA. *Biophys. J.* **87**: 105–112.

Yamada T, Fialho AM, Punj V, Bratescu L, Das Gupta TK, Chakrabarty AM. 2005. Internalization of bacterial redox protein Azurin in mammalian cells: entry domain and specificity. *Cell Microb.* **10**: 1418–1431.

Yamada T, Goto M, Punj V, Zaborina O, Chen ML, Kimbara K, Majumdar D, Cunningham E, Das Gupta TK, Chakrabarty AM. 2002a. Bacterial redox protein Azurin, tumor suppressor protein p53, and regression of cancer. *Proc. Natl. Acad. Sci. USA* **99**: 14098–14103.

Yamada T, Goto M, Punj V, Zaborina O, Kimbara K, Das Gupta TK, Chakrabarty AM. 2002b. The bacterial redox protein Azurin induces apoptosis in J774 macrophages through complex formation and stabilization of the tumor suppressor protein p53. *Infect. Immun.* **70**: 7054–7062.

Yamada T, Hiraoka Y, Ikehata M, Kimbara K, Avner BS, Das Gupta TK, Chakrabarty AM. 2004. Apoptosis or growth arrest: modulation of tumor suppressor p53's specificity by bacterial redox protein Azurin. *Proc. Natl. Acad. Sci. USA* **101**: 4770–4775.

Yamada T, Mehta RR, Lekmine F, Christov K, King ML, Majumdar D, Shilkaitis A, Green A, Bratescu L, Beattie CW, Das Gupta TK. 2009. A peptide fragment of Azurin induces a p53 – mediated cell cycle arrest in human breast cancer cells. *Mol. Cancer Ther.* **8**: 2947–2958.